SCIENCE CHINA
Technological Sciences

•Article•

July 2024 Vol.67 No.7: 2255–2273
https://doi.org/10.1007/s11431-023-2602-3

Screening current in ultra-high-field non-insulated superconducting magnets

ZHOU BenZhe[1,2], WANG Lei[2], CHEN Yong[1,2], WANG QiuLiang[1,2*], WANG KangShuai[1,2], ZHANG ZiLi[2] & LIU JianHua[1,2*]

[1] *University of Chinese Academy of Sciences, Beijing 100049, China;*
[2] *Institute of Electrical Engineering, Chinese Academy of Sciences, Beijing 100190, China*

Received August 7, 2023; accepted January 18, 2024; published online June 21, 2024

Screening current is recognized as one of the critical elements limiting the progression of superconducting magnets toward achieving higher magnetic fields. Currently, most non-insulated (NI) superconducting magnets consider the magnet as insulated when addressing the issue of screening current. However, the bypass current in the NI magnet can modify the actual history of magnetization, so the screening current in NI magnet will be different from that in the insulated magnet. This paper presents a novel method based on the homogenized **T-A** formulation (**T** is the current vector potential, and **A** is the magnetic vector potential), which enables real-time simulation of both the bypass current behavior and the implications of screening current in NI superconducting magnets, even when these magnets contain tens of thousands of turns. We have developed a 32 T NI hybrid superconducting magnet and validated the effectiveness of this method through experiments. Employing this efficacious method, we conducted a comprehensive calculation of screening current in NI magnets, comparing them with insulated magnets in terms of screening current-induced stress (SCIS), screening current-induced field (SCIF), and losses. The results indicate that in the NI insert coils, the sequential excitation of background coils and insert coils induces a reverse screening current, resulting in slightly lower SCIF and SCIS compared to those in the insulated magnets. The method and results can contribute to the enhancement of magnet design and provide valuable insights for the development of ultra-high fields (UHF) NI magnets.

ultra-high-field superconducting magnet, screening current, REBCO coil, NI coil, stress, loss

Citation: Zhou B Z, Wang L, Chen Y, et al. Screening current in ultra-high-field non-insulated superconducting magnets. Sci China Tech Sci, 2024, 67: 2255–2273, https://doi.org/10.1007/s11431-023-2602-3

1 Introduction

Superconducting magnets are highly prized in the realm of applications necessitating strong magnetic fields, including magnetic resonance imaging (MRI), nuclear magnetic resonance (NMR), and particle accelerators [1]. This preference is due to their characteristic high homogeneity, robust stability, low noise level, compact physical dimensions, and low power dissipation. Research in these application fields continually demands higher magnetic fields. The rare earth barium copper oxide (REBCO) coated conductors have emerged as the ideal choice for fabricating ultra-high-field superconducting magnets due to their excellent mechanical strength and high critical current density in high fields [2]. However, the large aspect ratio of REBCO coated conductors results in an increased screening current. Screening current not only diminishes the central magnetic field of the magnet but also induces spatial distortions and temporal drifts in the magnetic field distribution [3,4]. Furthermore, screening current exerts non-uniform Lorentz forces on the REBCO tapes [5], potentially causing overstress and irreversible damage [6], which presents a major

*Corresponding authors (email: qiuliang@mail.iee.ac.cn; liujianhua@mail.iee.ac.cn)

© Science China Press 2024

obstacle to the progression of superconducting magnets to higher magnetic fields. Various numerical methods have been proposed for the screening current, among which the finite element method (FEM) predicated on the **T**-**A** formulation [7] and a power-law model [8] of the superconductor has become the most favored method. This method can be easily implemented in commercial finite element software and enables real-time simulation of the entire magnet through enhanced multi-scale and homogenized variants [9]. Non-insulated (NI) technology [10] stands as an effective approach to attaining ultra-high field (UHF). NI coils do away with the insulation material between turns, enabling the current to bypass defects and course through adjacent turns, thereby preventing local hotspots that could potentially induce quenching. In addition, the elimination of insulation between turns augments the engineering current density and overall mechanical strength of the coil. Recent studies have underscored the significant potential of NI technology in UHF applications [11,12]. However, the introduction of a new dimension—bypass current, brings complexity to the analysis of the electromagnetic response of NI coils, which is not present in insulated coils. In recent years, researchers have put forth several equivalent circuit models to depict the bypass current behavior in NI coils, including lumped circuit models [10], two-dimensional (2D) axisymmetric circuit grid models [13], and partial element equivalent circuit models [14]. These models have successfully elucidated the self-protecting capability of NI coils and offered robust simulations of certain thermal stability and mechanical behaviors [15,16].

The accurate depiction of current density distribution and its variations proves crucial for NI high-field superconducting magnets, given its intimate relationship with magnetic field quality [17], losses [18], stress, and strain [19]. Nevertheless, research that simultaneously addresses both bypass current and screening current in NI superconducting magnets remains scarce. Most studies on screening current in NI superconducting magnets generally utilize steady-state calculation models akin to those for insulated magnets, predicated on the assumption that the bypass current has decayed to zero [20]. However, this assumption has made an oversimplification. The well-established fact that the screening current in a superconductor carries a historical dependence on the excitation path [21,22], while bypass currents can modify the actual excitation path within the NI superconducting magnets, implies that the screening current in NI superconducting magnets may differ from that in insulated superconducting magnets. The commonly used approach is to initially calculate the azimuthal current employing an equivalent circuit model for each turn, and then harness the azimuthal current as a boundary condition for the calculation of screening current. This methodology, nonetheless, introduces some errors in the interplay between screening current and bypass current. A few years back, our research group grappled with the constraints of this approach and proposed a refined circuit model [23]. Within this model, each azimuthal element in the NI superconducting coil is superseded by a cluster of axially subdivided azimuthal elements to emulate the variation of current along the width direction of the superconducting tape. Similar refined circuit models have also been recommended in ref. [24] for simulating the screening current in NI superconducting coils. However, these methods necessitate substantial computational time to compute the accurate dynamic inductance matrix and involve bespoke programming, rendering it inconvenient for coupling analysis with other fields such as stress and temperature fields. FEMs offer convenient multi-physics analysis in commercial software. Lately, an FEM based on the **H**-formulation and rotated anisotropic resistivity has been proposed [25], facilitating simultaneous analysis of screening current and bypass current in the NI superconducting coil. However, for ultra-high-field NI superconducting magnets comprising tens of thousands of turns, this method still encounters difficulties in applying external constraints via an external power source, and the computational time remains a challenge to satisfy. It may take tens of days even if acceleration methods such as homogenization or iterative multi-scale are used [26]. Otten et al. [27] initially simplified a partially coupled Roebel cable to compute its alternating current (AC) losses, treating it as an anisotropic single block. They then adopted common integration methods and certain constraint conditions to determine one component of the current density J_x. The correlation between the two components of the current density, J_x and J_z, was established, enabling the ascertainment of the entire current density. Based on this idea, this study presents a method for calculating screening current in NI superconducting coils. This method also treats NI superconducting coils as anisotropic single blocks with the transformation method [25]. Subsequently, we derive an expression for the relationship between radial current density and azimuth current density by using Faraday's law of electromagnetic induction when the coil structure is transformed. Consequently, the boundary conditions including radial current density in the **T**-**A** formulation are deduced. Partial differential equations (PDEs) relating to current vector potential **T** and magnetic vector potential **A** are established using the commercial finite element software COMSOL Multiphysics, which enables the simultaneous simulation of bypass current behavior and the effects of screening current. This novel method provides a more precise depiction of the current density distribution in NI UHF superconducting magnets, thereby serving as a significant foundation for analyzing magnetic field quality, losses, stress, and so on.

2 Numerical model

2.1 Anisotropic monoblock model

High-field superconducting magnets are typically assembled from an array of double-pancake (DP) coils. Each DP coil is a complex 3D structure with nearly axisymmetric characteristics, consisting of extremely thin REBCO tapes. These REBCO tapes are spirally wound from the center, forming two individual pancake coils with radial outward spirals—one wound upward and the other downward. A continuous transition region with lateral bending is formed at the inner diameter connection where these two single pancake (SP) coils connect. The REBCO tape is a multilayer composite material composed of a Hastelloy alloy substrate, a buffer layer, a silver layer, a copper stabilizer layer, and a superconducting layer. Each layer has distinct electromagnetic and mechanical properties, but they can be considered periodically arranged in the coil. While the complex 3D structure composed of thin-walled sections can be simplified using quasi-3D modeling—a technique validated in racetrack coils [28] and certain cables, the computational complexity remains considerable for large-scale ultra-high-field superconducting magnets with tens of thousands of turns. Consequently, further simplification to 2D modeling becomes necessary.

When simplifying the REBCO coil, the transition turns at the inner diameter, and the joints at the outer diameter of the DP coil are initially disregarded, thereby treating the DP coil as two independent spiral SP coils. Then, the multilayer material with isotropic resistivity is transformed into a single material with anisotropic resistivity through homogenization. Under normal operating conditions, the NI superconducting coils behave as a superconductor in the direction parallel to the superconducting tapes and exhibit resistive behavior in the direction perpendicular to the tapes. The resistivity of the superconductor denoted as $\rho_{\parallel}$, adheres to the **E-J** power-law relationship:

$$\rho_{\parallel} = \frac{E_c}{J_c(B)} \left| \frac{J}{J_c(B)} \right|^{n(B)-1}. \tag{1}$$

The resistive behavior exhibited in the direction perpendicular to the superconducting tapes is represented by $\rho_{\perp}$. It is related to the resistivity of the metal layers, the interface resistivity, and the contact resistivity, all of which can be determined through experimental measurements. Under steady-state conditions, only currents parallel to the tape's plane exist. Due to the significantly lower resistance of the thin superconducting layer compared to other parts (such as the alloy substrate or copper stabilizer layer), parallel currents are confined to the thin superconducting layer and cannot pass through other layers. However, in practical coils, a phenomenon of parallel current shunting may occur. When the parallel current surpasses the critical current, causing the superconducting layer to transition to the normal state, it begins to diffuse into nearby metal layers. If all the currents were obliged to flow within the superconducting layer, the electric field within the superconducting layer would be much higher than the actual field. In this model, we postulate that there is no parallel current shunting under steady-state conditions. However, under non-steady-state conditions, all bypass currents are regarded as perpendicular currents.

For any point in the actual spiral coil's coordinate system, a transformation into an axisymmetric coordinate system can be achieved through a local rotation of the coordinates by a specific angle. The relationship between the current density and electric field in the original and transformed coordinate systems is as follows:

$$\begin{bmatrix} J_{\parallel} \\ J_{\perp} \end{bmatrix} = \begin{bmatrix} \cos(\alpha) & -\sin(\alpha) \\ \sin(\alpha) & \cos(\alpha) \end{bmatrix} \begin{bmatrix} J_{\varphi} \\ J_{r} \end{bmatrix}, \tag{2}$$

$$\begin{bmatrix} E_{\parallel} \\ E_{\perp} \end{bmatrix} = \begin{bmatrix} \cos(\alpha) & \sin(\alpha) \\ -\sin(\alpha) & \cos(\alpha) \end{bmatrix} \begin{bmatrix} E_{\varphi} \\ E_{r} \end{bmatrix}, \tag{3}$$

where the subscripts $\parallel$ and $\perp$ denote the tangential and normal components in the coordinate system of the spiral model, respectively, corresponding to the directions parallel and perpendicular to the superconducting tapes in the spiral single-pancake coil. In the axisymmetric coordinate system, the directions of the parallel and perpendicular superconducting tapes correspond to the azimuth and radial directions, respectively, and thus are denoted by subscripts φ and r. The transformation of physical quantities remains independent of the axial coordinate z.

We assume that the coil follows the form of an Archimedean spiral, which can be expressed by the following equation:

$$r = r_1 + \frac{r_2 - r_1}{2\pi}\theta, \tag{4}$$

where r_1 denotes the inner radius, r_2 represents the outer radius, and θ corresponds to the azimuthal direction. The angle α, necessary for the local coordinate rotation, is determined by the dimensions of the coil as follows:

$$\alpha = \pm\sin^{-1}\left(\frac{d}{2\pi r}\right), \tag{5}$$

where d is the thickness of the superconducting tape, r is the radius at the specific position, and $\pm$ signifies the direction of the spiral.

In the coordinate system of the spiral model, the constitutive relation can be expressed as follows:

$$\begin{bmatrix} E_{\parallel} \\ E_{\perp} \end{bmatrix} = \begin{bmatrix} \rho_{\parallel} & 0 \\ 0 & \rho_{\perp} \end{bmatrix} \begin{bmatrix} J_{\parallel} \\ J_{\perp} \end{bmatrix}. \tag{6}$$

In the 2D axisymmetric coordinate system, eqs. (2) and (3) can be substituted into eq. (6) to obtain the constitutive relation as follows:

$$E_\varphi = J_\varphi\left(\rho_\parallel \cos^2(\alpha) + \rho_\perp \sin^2(\alpha)\right) + J_r(\rho_\perp - \rho_\parallel)\sin(\alpha)\cos(\alpha), \tag{7}$$

$$E_r = J_\varphi(\rho_\perp - \rho_\parallel)\sin(\alpha)\cos(\alpha) + J_r\left(\rho_\perp \cos^2(\alpha) + \rho_\parallel \sin^2(\alpha)\right). \tag{8}$$

For computational convenience, we can define equivalent azimuthal resistivity ρ_φ and equivalent radial resistivity ρ_r:

$$\rho_\varphi = \rho_\parallel \cos(\alpha)(\cos(\alpha) + \sin(\alpha)) + \rho_\perp \sin(\alpha)(\sin(\alpha) - \cos(\alpha)), \tag{9}$$

$$\rho_r = \rho_\perp \cos(\alpha)(\cos(\alpha) - \sin(\alpha)) - \rho_\parallel \sin(\alpha)(\cos(\alpha) + \sin(\alpha)). \tag{10}$$

2.2 Homogenized *T-A* formulation

The calculation of the screening current within the superconducting coil employs the widely utilized homogenized **T-A** formulation in the 2D axisymmetric coordinate system. Within the superconducting domain, the current density **J** is calculated using the current vector potential **T** as the variable, while across the entire domain, the magnetic vector potential **A** is employed to calculate the magnetic flux density **B**. In the 2D axisymmetric coordinate system, the magnetic vector potential **A** possesses only an azimuthal component A_φ, and the superconducting layer is considered as a 1D thin slice with negligible thickness. Therefore, **T** possesses only one component T_r. The governing equations for **T** and **A** are as follows:

$$\nabla^2 A_\varphi = -\mu_0 J_\varphi, \tag{11}$$

$$\frac{\partial}{\partial z}\left(\rho_\varphi \frac{\partial T_r}{\partial z}\right) = \frac{\partial B_r}{\partial t}. \tag{12}$$

The boundary condition for T_r at the edge of the 1D superconducting layer can be deduced by integrating the azimuthal current density J_φ across the cross-section, which represents the current supplied by the power source:

$$I = \iint_S J \mathrm{d}S = \iint_S \nabla \times T \mathrm{d}S = \oint_l T \mathrm{d}l, \tag{13}$$

where S is the cross-section of the superconducting layer and l is the boundary of the cross-section. Since the superconducting layer is considered 1D, eq. (13) can be written as

$$I = (T_1 - T_2)\delta, \tag{14}$$

where δ is the actual thickness of the superconducting layer, and T_1 and T_2 are the current vector potentials at their respective edges. The boundary conditions for T_r are typically written as

$$T_1 = \frac{I}{\delta}, \tag{15}$$

$$T_2 = 0. \tag{16}$$

Figure 1(c) shows the homogenized approach applied to a small stack. The homogenized **T-A** formulation scales the geometrical dimensions of multiple turns of the superconducting layer within the same coil to the dimensions of a single superconducting tape in the radial direction, merging all the superconducting layers into a 2D block. However, the calculations do not consider the influence of B_z, and the control equation for the 1D superconducting layer remains the same. For each superconducting layer in the 2D block, its current is consistent with the original 1D superconducting tape. Hence, the boundary conditions eqs. (15) and (16) for T_r are applied to the top and bottom edges of the 2D block. As the dimensions of the superconducting layers are scaled up, a proportional relationship between the engineering azimuthal current density $J_{e\varphi}$ used in the calculation of magnetic flux density **B** and the actual azimuthal current density J_φ in the superconducting layer as follows:

$$J_{e\varphi} = \frac{\delta}{d} J_\varphi, \tag{17}$$

where d is the thickness of the superconducting tape. Ref. [29] provides further detailed descriptions of the homogenized **T-A** formulation.

2.3 The constraint of radial current density J_r

In the 2D axisymmetric coordinate system, the current density in the NI coil consists of two components. However, the homogenized **T-A** formulation solely solves for the component J_φ. Therefore, it is necessary to ascertain the relationship between the component J_r and the component J_φ through constraint conditions. Since the magnet is driven by external current sources, the total current density in each series-connected single-pancake coil is governed by the external operating current. According to Faraday's law of electromagnetic induction, we get

$$\frac{\partial \mathbf{A}}{\partial t} = -\mathbf{E} - \nabla \phi, \tag{18}$$

where ϕ is the scalar potential.

Figure 1(a) illustrates the actual topology of an NI coil, where for any turn, the potential difference along the path l_{acb} is equal to that along the path l_{adb}. The simplified model alters the topological structure of the subject being modeled. In the 2D axisymmetric coordinate system, an SP coil is represented not as a spiral but as a series of radially connected concentric circles, as demonstrated in Figure 1(b). This model simplification maintains the electromagnetic relationship intact. Therefore, we postulate that in the 2D axisymmetric structure, the potential difference between any two points along different paths remains the same, with the radial and azimuthal directions selected as the paths. As the

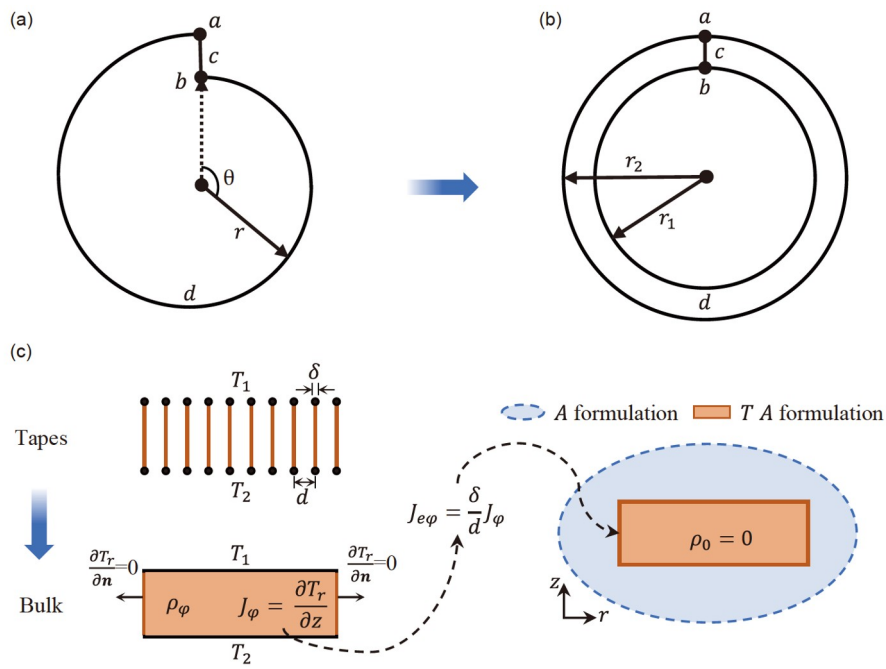

Figure 1 (Color online) The schematic diagram of the homogenized **T**-**A** formulation of the NI coil. (a), (b) The structural transformation of NI coil. Without modifying the electromagnetic relationship within the NI coil, its structure in the 2D axisymmetric coordinate system transitions from a spiral shape into a series of concentric circular rings. (c) **T**-**A** homogeneous approach.

radial current does not generate a magnetic field, we can derive the following relationship from eq. (18):

$$J_r = \frac{2\pi r \cdot \left(\frac{\partial A_\varphi}{\partial t} + \rho_\varphi J_\varphi\right)}{d \cdot \rho_r}. \tag{19}$$

Currently, J_r can be represented as a function of J_φ. By combining eqs. (15) and (19), we derive the Dirichlet boundary conditions for the **T**-**A** formulation of the NI superconducting coil as follows:

$$T_1 = \frac{I_{op} - 2\pi r \int_{z_1}^{z_2} \frac{2\pi r \cdot \left(\frac{\partial A_\varphi}{\partial t} + \rho_\varphi J_\varphi\right)}{d \cdot \rho_r} \mathrm{d}z}{\delta}, \tag{20}$$

$$T_2 = 0, \tag{21}$$

where I_{op} is the operational current.

In the commercial finite element software like COMSOL Multiphysics, two PDEs can be established for **A** and **T**, and an additional PDE can be used to solve the spatial integration present in the boundary conditions. Since it is impossible to impose pointwise constraints on the time derivative of the dependent variable at each grid node in COMSOL Multiphysics, another PDE can be employed to solve $\frac{\partial A_\varphi}{\partial t}$. Hence, computing the screening current in an NI superconducting coil requires four PDEs. This approach, while easy to understand and implement, consumes more computational time compared to the two PDEs required for insulated superconducting coils.

An alternative advanced approach employs the component coupling operators and weak constraints. The domain can be projected onto the boundary in the z-direction via a generalized projection operator to perform spatial integration in the boundary conditions. Weak constraints are applied through local averaging, utilizing shape functions as weights, which permits the same variable as other terms in the coupled equation system. Eq. (20) exhibits strong nonlinearity, and the solution of the linearized sub-problems in each solver step relies on the values of the Lagrange multiplier variables from the preceding step. Through weak constraints, the values of the Lagrange multipliers can be maintained between steps, fostering faster and more robust convergence. This approach demands a deeper understanding of COMSOL Multiphysics and involves more complex operations. However, it only necessitates the establishment of two PDEs. The computational speed can be almost on par with the conventional homogenized **T**-**A** formulation for insulated superconducting coils.

3 Experimental verification

3.1 Parameters of a 32 T hybrid high-low temperature superconducting NI magnet

To validate the effectiveness of this model, a 32 T NI high-low temperature hybrid superconducting magnet was developed and tested. Figure 2 presents the overall structure of

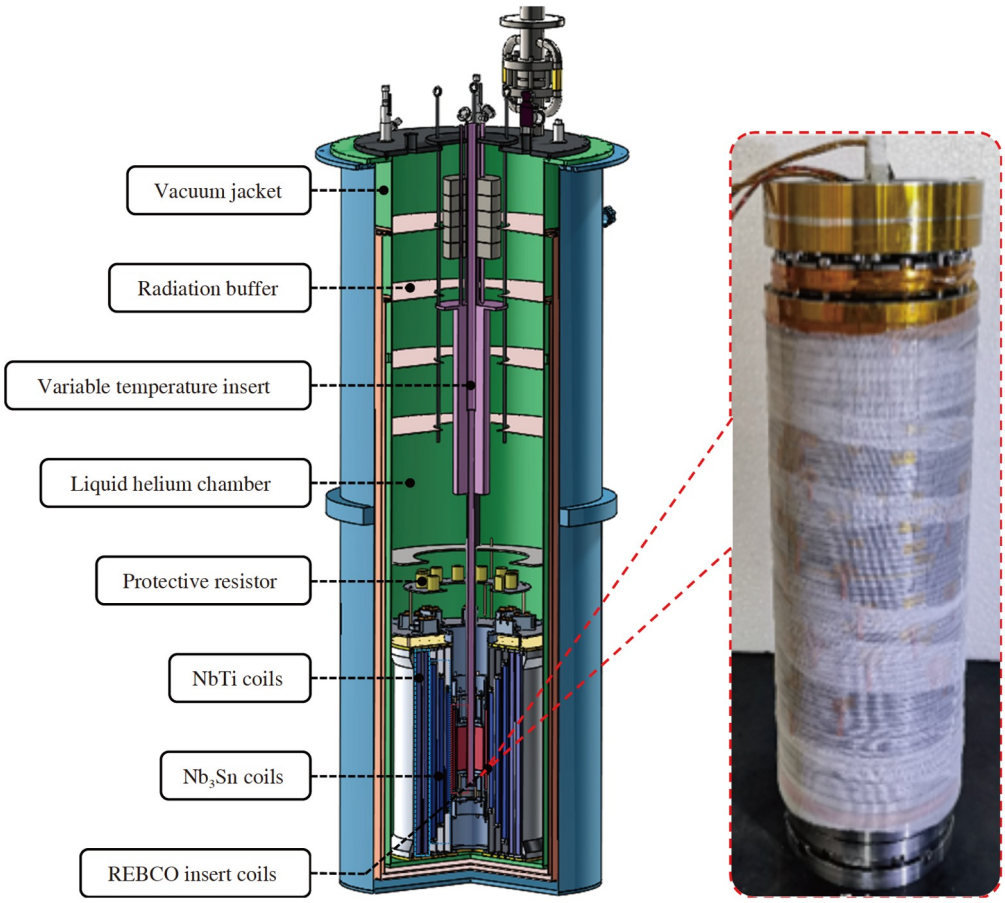

Figure 2 (Color online) Schematic diagram of the 32 T high-low temperature hybrid superconductor magnet system and a photograph of the NI REBCO insert coil.

the magnet system and a photo of the insert magnet. The background field magnet utilizes insulated low-temperature superconducting (LTS) technology, featuring a central magnetic field strength of 15 T and a diameter of 160 mm. It consists of three internal Nb_3Sn coils and four external NbTi coils. Detailed parameters can be found in Table 1. The insert magnet, on the other hand, is a 17 T NI REBCO high-temperature superconducting (HTS) magnet with a diameter of Ø35 mm. It is comprised of 56 DP coils arranged in inner and outer layers, consisting of seven different types. The specific parameters of the insert magnet refer to the reference [11].

A series of experiments were conducted on the NI REBCO insert coils in liquid nitrogen, which were then followed by experiments executed on the entire magnet system in liquid helium. Simulations were performed to emulate the actual excitation process, with the resultant data compared against corresponding experimental findings. A parameter-free method proposed in ref. [30] was employed to extract the angle dependence of the critical current of the REBCO tapes in liquid nitrogen based on experimental measurements. A fitting formula from ref. [31] is utilized to describe the angle dependence of the critical current at liquid helium temperature. To facilitate the modeling process, the form of $I_c(B,\theta)$ was transformed to $I_c(B_{\parallel},B_{\perp})$ and subsequently normalized to the critical current of REBCO tape with a width of 4 mm. For the field angle dependence of the *n*-value, the *n*-values at 77 K are sourced from the Robinson Institute's database. [32] At 4.2 K, the *n*-values in the range of 0–8 T are also obtained from the Robinson Institute's database, while the *n*-value at 19 T is derived from ref. [33]. Limited research or experimental data exist for *n*-values under conditions other than 19 T. Consequently, in the simulations presented in this paper, the *n*-values for higher magnetic fields are extrapolated by interpolating the available data at 19 T. The data of the angle dependence of the critical current and *n*-value are shown in Figure 3.

3.2 Individual experiments of NI REBCO insert coil at 77 K

We first tested the critical current of the NI REBCO insert coil at 77 K. The insert coil was placed separately in liquid nitrogen, and a series of ramp-hold operations were conducted on the excitation current. During the ramp phase, the ramping rate was set at 0.0107 A/s, which was then followed by a one-hour hold phase. The excitation current was

Table 1 Paraments of the LTS background field magnet of the 32 T superconducting magnet

Parameter	Unit	LTS background field coils						
		Coil 1	Coil 2	Coil 3	Coil 4	Coil 5	Coil 6	Coil 7
		Nb_3Sn			NbTi			
Inner radius	mm	92	110	124.2	142.8	158.2	175.2	190.9
Outer radius	mm	108	120.6	141.1	154.87	174.2	187.2	221.3
Height	mm	280	260	320	400	260	240	400
Engineering current density J_e	A/mm^2	115.689	116.338	137.612	103.654	136.697	123.675	193.350
Central field	T				15			
Operating current	A				215			
Inductance	H				111.93			
Storage energy	MJ				2.61			

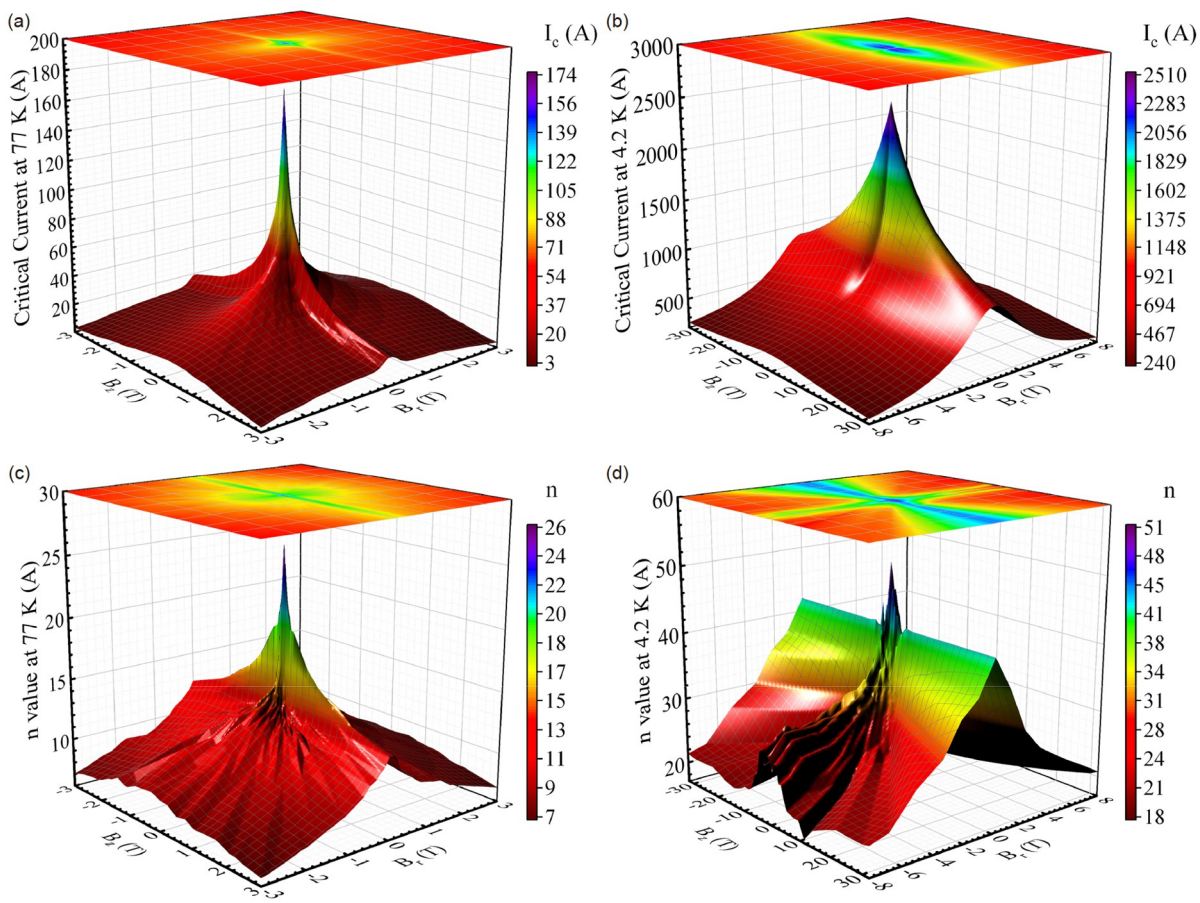

Figure 3 (Color online) The angle dependence of the critical current and *n*-value of the REBCO tape used in the simulation. (a) I_c at 77 K; (b) I_c at 4.2 K; (c) *n*-value at 77 K; (d) *n*-value at 4.2 K.

increased continuously, and the voltage signals of all DP coils were measured until the terminal voltage of one of the coils reached the critical current criterion of 0.1 μV/cm. The test results indicated the critical current of the NI REBCO insert coil is 28.2 A at 77 K.

Subsequently, two experiments were conducted at target currents of 10 and 20 A, following the experimental procedure outlined below: (1) The excitation current was gradually increased to the target current at a ramping rate of 0.0107 A/s; (2) the excitation current was maintained at the target level for at least 1 h, waiting for the radial current to completely decay; (3) the magnetic field distribution along the central axis, from −150 to 150 mm, was measured using a spatial field mapping system; (4) a sudden discharge was

performed, and the time constant of the NI coil was measured; (5) the excitation current was maintained at 0 A for at least 1 h, waiting for the radial current to completely decay; (6) the remnant magnetic field distribution along the central axis, from −150 to 150 mm, was measured using a spatial field mapping system.

Throughout the entirety of the experiment process, the central magnetic field and the voltage signals at the coil terminals were continuously recorded. The inter-turn resistivity of the REBCO insert coil in liquid nitrogen was measured to be 11.7 μΩ cm^2. It should be noted that before conducting the critical current test, as well as the 10 and 20 A experiments, the REBCO insert coil was restored to room temperature and re-cooled to avoid any influence from the remnant magnetic field on the initial magnetic field for subsequent experiments.

Figure 4 presents the experimental data, as well as the simulation results obtained from both the proposed NI coil's screening current calculation model and the axisymmetric equivalent circuit model. It can be observed that both the voltage and magnetic field simulated by the NI coil's screening current calculation model exhibit similar delayed effects as those simulated by the axisymmetric equivalent circuit model. In the current-ramping phase, the axisymmetric equivalent circuit model's simulated voltage is slightly higher than that from the NI coil's screening current calculation model. The difference may be attributed to the change in inductance induced by the screening current, resulting in inductance voltage variations. It is noteworthy that these variations can be accurately computed by the NI coil's screening current calculation model. Furthermore, due to the axisymmetric equivalent circuit model's inability to simulate screening current, the magnetic field that it simulates is unaffected by the screening current-induced field (SCIF). This results in an elevated central magnetic field during the current-holding phase and a decrease to zero after sudden discharge, without displaying a remnant field as observed in the experimental data. In contrast, the NI coil's screening current

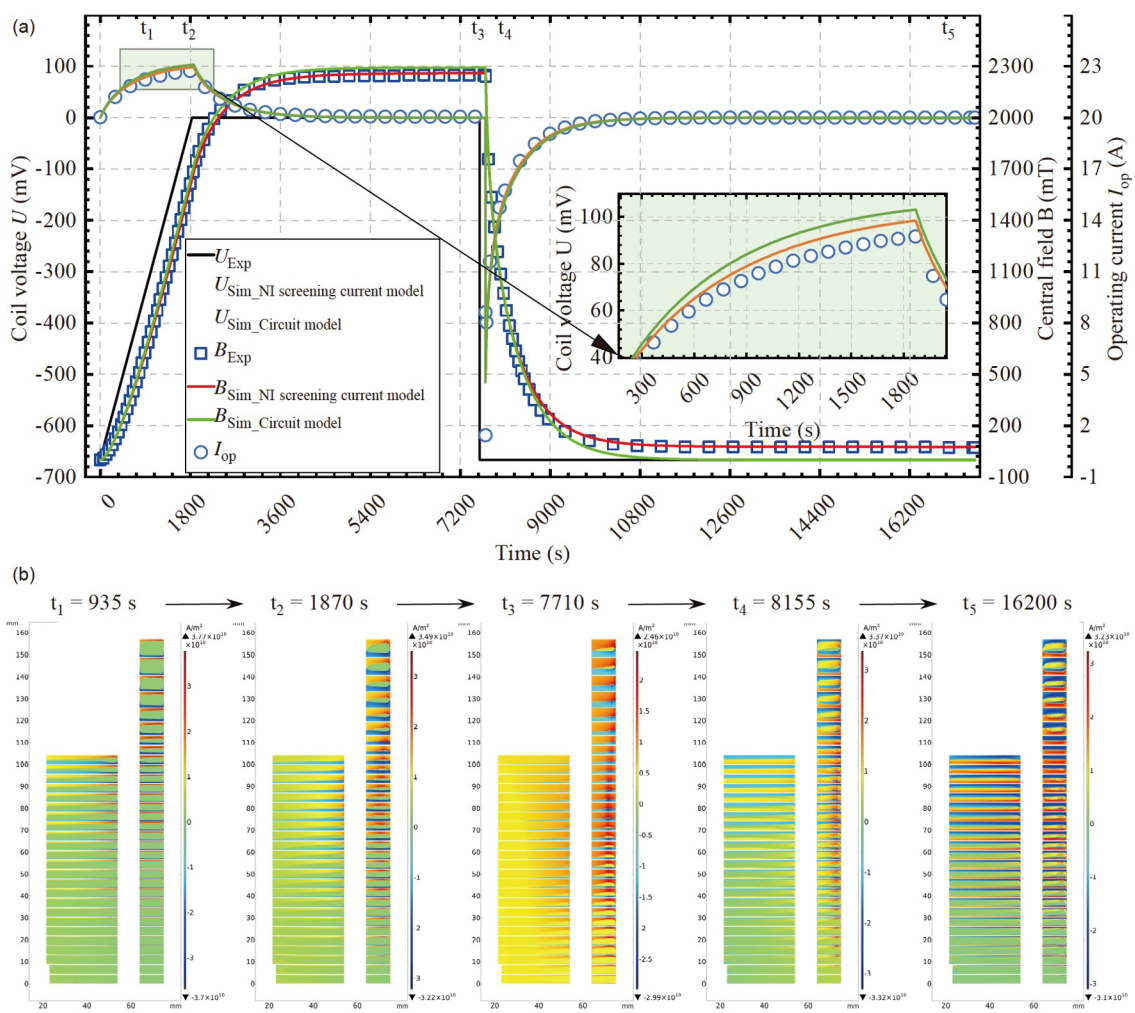

Figure 4 Liquid nitrogen experiments at a target current of 20 A. (a) Comparison of voltage and magnetic field of experimental measurements, simulation of the 2D axisymmetric circuit grid model and the NI coil's screening current model. (b) Distribution of the azimuthal current density at different time simulated by the NI coil's screening current model.

calculation model accurately simulates the SCIF and remnant magnetic field, which are in better agreement with the experimental results. During the sudden discharge phase, both the axisymmetric equivalent circuit model and the NI coil's screening current calculation model show significant deviations in voltage simulation compared to the experimental data, which may be attributed to inter-turn resistance changes caused by factors such as stress.

Figure 5 illustrates both the simulated and experimental distributions of remnant magnetic field and the SCIF along the central axis. For an NI superconducting coil, once the radial currents have completely decayed, the discrepancy between the actual and ideal fields can be solely attributed to the effect of screening current. Thus, the SCIF can be represented by the discrepancy between the actual and ideal fields. The simulated SCIF corresponds closely with the experimental results, demonstrating an "M"-shaped distribution along the central axis, with negative values close to the central plane of the coil and positive values farther away. In proximity to the central plane of the coil, the magnitude of the SCIF from the 10 A experiment exceeds that from the 20 A experiment, given that the 20 A experiment nears the coil's critical current, thereby suppressing the screening current. The remnant magnetic field is directly generated by screening current and is independent of the ideal field. The model's effectiveness can be further validated by comparing the experimental and simulated remnant magnetic fields. The simulated remnant magnetic field corresponds closely with the experimental results, exhibiting a "W"-shaped distribution along the central axis that is the reverse of the SCIF. Near the central plane of the insert REBCO coil, the magnitude of the remnant magnetic field from the 20 A experiment exceeds that from the 10 A experiment, owing to more flux penetration occurring during the process of reducing the current from 20 to 0 A. Both the remnant field and the SCIF exhibit asymmetry in experimental measurements, presenting some discrepancies when compared to the simulation, possibly due to the asymmetric of the critical currents [34].

3.3 Experiments of the 32 T hybrid superconducting magnet at 4.2 K

We conducted tests on the NI REBCO insert coil which was housed within the LTS background field coil submerged in a liquid helium bath. Initially, the NI REBCO insert coil was independently excited to generate a central magnetic field of 12 T, as an initial system check. Subsequently, it was discharged, as shown by the peak between 2 and 6 h in Figure 6. After a waiting period of around 40 h, the LTS background field coil was excited to 15 T, followed by the excitation of the NI REBCO insert coil. Finally, the current of the NI REBCO insert coil was excited to the target level, and after holding the target current for approximately half an hour, the central magnetic field achieved 32.35 T.

We simulated the entire excitation process in liquid helium using an inter-turn resistivity of μΩ cm^2. Figure 7 illustrates both the simulated and experimentally measured central magnetic fields. Due to the significant influence of contact pressure on the contact resistivity, but the simulation model employed in this study did not account for variations in contact pressure during the excitation process. As a result, there is a slight discrepancy between the simulated and experimental curves of the central magnetic field. However, the simulation still captures the delayed effect caused by the radial current and the remnant field caused by the screening current. The rotation effect of the tape under UHF, which can

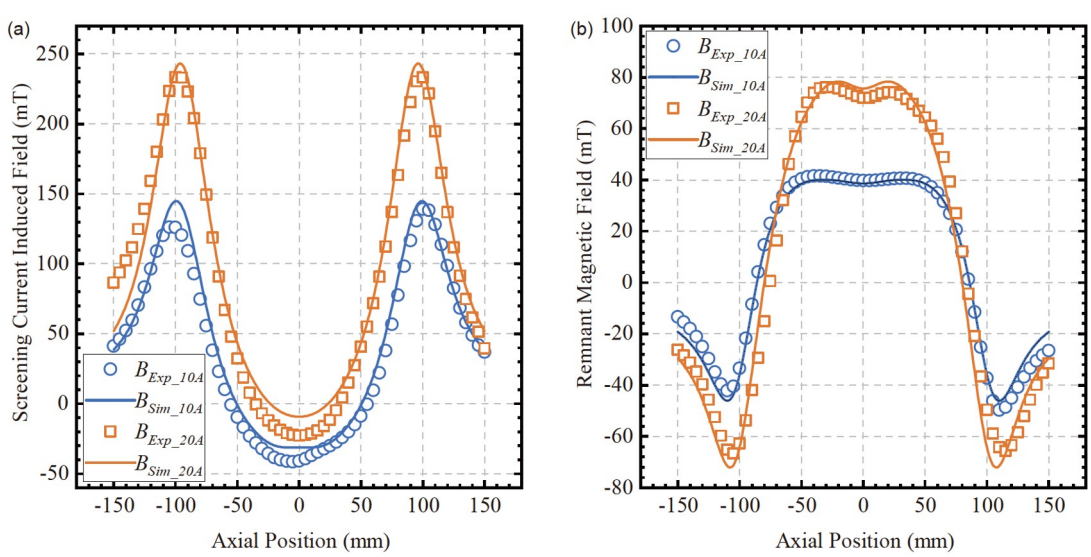

Figure 5 (Color online) Comparison of experimental and simulated axial magnetic field distribution in liquid nitrogen with target currents of 10 and 20 A respectively. (a) Comparison of fields induced SCIF. (b) Comparison of the remnant magnetic field.

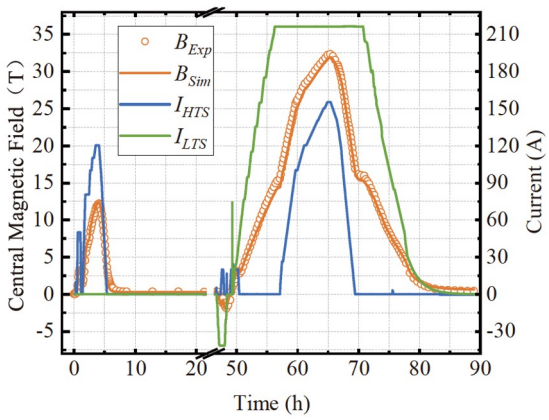

Figure 6 Experimental and simulated magnetic field throughout the entire process of liquid helium experiments. I_{HTS} and I_{LTS} represent the operating currents for the HTS magnet and the LTS magnet, respectively.

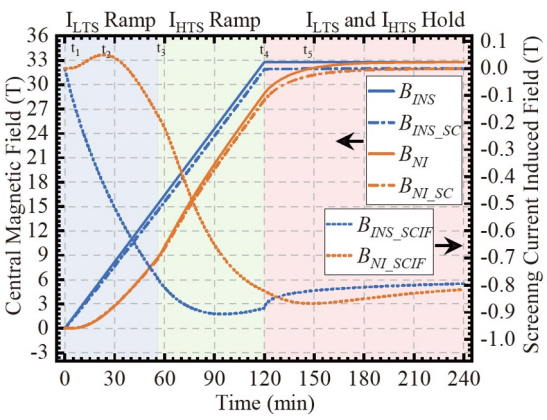

Figure 7 Central magnetic field and SCIF in NI and insulated magnets under various conditions.

alter the angle between the magnetic field and the tape and affect the screening current, was not considered in the model. Consequently, the simulated remnant field is slightly higher than the measured remnant field in the experiment.

4 Comparison of screening currents between NI superconducting magnets and insulated superconducting magnets

In this section, we will focus on the simulation of the 32 T high-low temperature hybrid superconducting magnet (detailed in Section 3). We aim to provide an in-depth computation of the distribution and variation of screening currents in NI superconducting magnet. Furthermore, we will juxtapose the discrepancies in screening current-induced stresses, SCIFs, and losses between NI and insulated superconducting (INS) magnets operating under identical conditions and with similar parameters.

4.1 Reverse screening currents in NI superconducting magnets

Considering that the LTS background coil and HTS insert coil are not serially connected, we persist with an independent excitation approach for our simulation. Initially, the LTS background coil is excited to the target current of 215 A at a ramping rate of 3.8926 A/min. Subsequently, the HTS insert coil is excited to a target current of 155 A at a ramping rate of 2.3932 A/min. The entire process takes approximately 2 h. Figure 7 illustrates the central magnetic field variation (left axis) under four different scenarios: (1) Assuming the REBCO insert coil is an insulated coil without considering the screening current, the central magnetic field is denoted as B_{INS}. If coil manufacturing errors and force-induced deformations in the magnet are not considered, B_{INS} represents the ideal design magnetic field. (3) Assuming the REBCO insert coil is an insulated coil with consideration of the screening current, the central magnetic field is denoted as $B_{INS.SC}$. (2) Assuming the REBCO insert coil is an NI coil without considering the screening current, the net central magnetic field is denoted as B_{NI}. (4) Assuming the REBCO insert coil is an NI coil with consideration of the screening current, the central magnetic field is denoted as $B_{NI.SC}$.

For clarity in the subsequent discussion, it is necessary to elaborate on the SCIF of NI superconducting magnets. In a conventional insulated superconducting magnet, the radial component of the magnetic field penetrates a wide region of the superconducting tape when the insulated magnet is excited, which generates the screening current. The distribution of the screening current density is extremely uneven, displaying a gradient pattern along the width of the superconducting tape (i.e., the axial direction of the superconducting magnet). The uneven current density distribution culminates in severe magnetic field distortion, and the actual central magnetic field $B_{INS.SC}$ is slightly diminished relative to the ideal design magnetic field B_{INS}. The portion of the magnetic field reduced, ΔB_{INS}, also known as the SCIF, is the field generated by the screening current relative to the coil transport current. For insulated magnets, the screening current-induced field is denoted as $B_{INS.SCIF} = B_{INS.SC} - B_{INS}$. Unlike insulated magnets, the difference ΔB_{NI} between the actual central magnetic field and the ideal design magnetic field in an NI magnet during excitation consists of two parts. In addition to the SCIF $B_{NI.SCIF}$ caused by the gradient distribution of the current density in the axial direction, there is also a magnetic field delay B_{delay} caused by the radial current. In this study, we define the difference field for the NI superconducting magnet as $\Delta B_{NI} = B_{INS} - B_{NI.SC}$, the SCIF as $B_{NI.SCIF} = B_{NI.SC} - B_{NI}$ and the delayed magnetic field as $B_{delay} = B_{INS} - B_{NI}$.

The SCIF during the excitation process of the insulated magnet, depicted in Figure 7 (right axis), remains consistently negative. As the excitation current increases, the SCIF's magnitude first expands and then contracts. This fluctuation can be explained by the current density and magnetic field distribution illustrated in Figure 8 during the excitation process of the insulated superconducting magnet. When both the background coil and the inserted coil are charged, an outward radial magnetic field is generated, prompting magnetic flux to penetrate the HTS tape on both sides. The current density on the side further from the magnet's center plane reaches positive critical current density, while the side closer to the center plane attains negative critical current density (for ease of description, we refer to the side further from the center plane as the "outer side" and the closer side as the "inner side"). As the radial magnetic field increases, so does the penetration depth, while the critical current density decreases with the escalation of the external magnetic field strength. When the magnetic flux has not fully penetrated, the increase in penetration depth primarily contributes to the magnitude of the SCIF, which escalates with the external magnetic field. Upon the full penetration of the magnetic flux into the superconducting tape, the reduction in critical current density becomes dominant, significantly influencing the SCIF magnitude. When the excitation current reaches the target value, the screening current experiences a relaxation change, leading to a sudden alteration in the rate of change of the SCIF magnitude, followed by a gradual reduction in the SCIF magnitude.

The SCIF in the NI superconducting magnet, as shown on the right axis of Figure 7, follows a completely different trend from that of the insulated superconducting magnet. At the initial excitation of the background field coil, the value of the SCIF in the NI superconducting magnet is positive, contrary to the usual negative. With the increase of the background field, the amplitude of the SCIF first increases, then decreases and gradually changes to negative. After the start of the excitation of the inserted coil, the value of the SCIF remains negative. Its amplitude will increase with the increase of the excitation current, and then gradually decrease. The distribution of current density and magnetic field during the excitation process of the NI superconducting magnet is shown in Figure 9.

When the excitation of the background field coil just begins, an azimuthal current is induced in the insert coil. The direction of this current is opposite to that of the current applied by the power source. The outer inserted coil

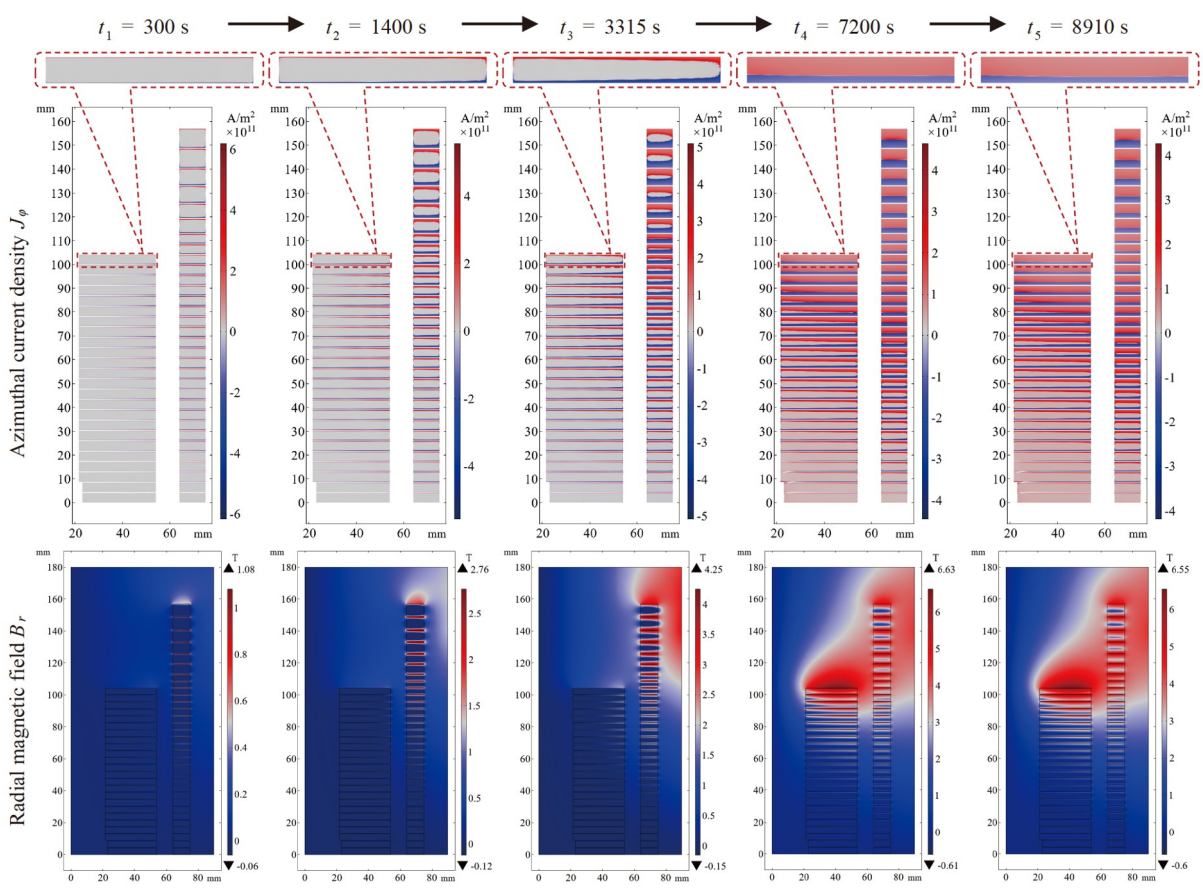

Figure 8 (Color online) Azimuthal current density distribution and radial magnetic field distribution at different moments during the excitation process of the insulated superconducting magnet.

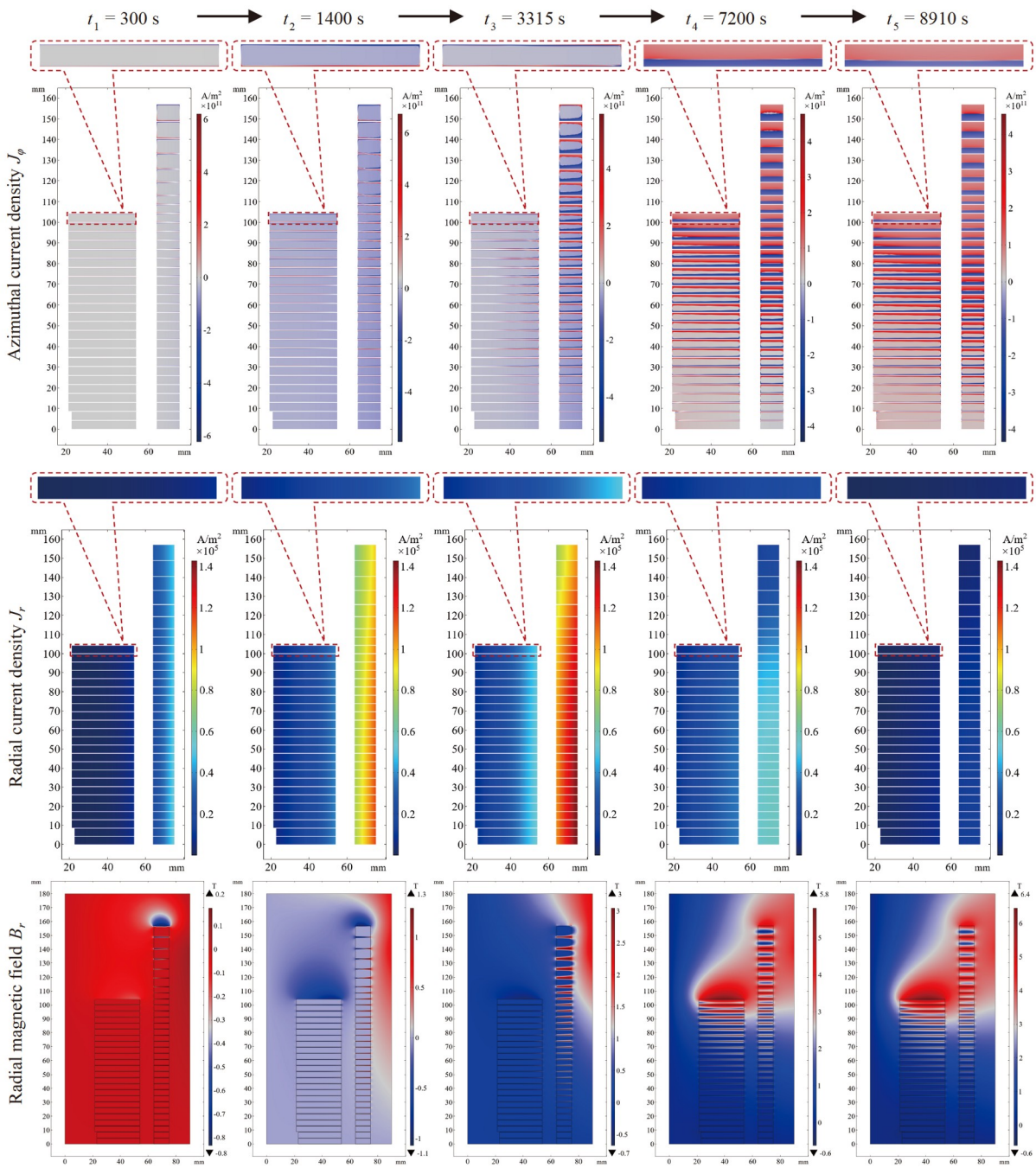

Figure 9 (Color online) Azimuthal current density, radial current density, and radial magnetic field distribution at different moments during the excitation process of the NI superconducting magnet.

primarily induces a reverse current, and the magnetic field generated by the reverse current causes the local magnetic field near the end of the outer inserted coil to change to inward radial. The distribution of current density also contradicts the usual distribution: the current density on the outer side reaches negative critical current density, while the inner side reaches positive critical current density. Therefore, the magnetic field near the middle plane is larger than the ideal magnetic field, while near the end coil is smaller. As the background field intensifies, the reverse current in the outer insert coil also increases. Consequently, the radial inward magnetic field strengthens, the penetration depth increases, and the amplitude of the SCIF also increases.

As the background field continues to intensify, the rate of increase of the azimuthal current induced in the outer insert coil slows down, and a reverse azimuthal current gradually is induced in the inner insert coil. However, since the reverse azimuthal current induced in the inner insert coil is small, the

inward radial magnetic field it produces is weaker than the outward radial magnetic field generated by the background field. The amplitude of inward radial magnetic field decreases and gradually inverts to an outward orientation. The screening current density also starts conforming to the distribution rule of the insulated superconducting magnet. Therefore, the amplitude of the SCIF decreases and then turns negative, mirroring subsequent changes in the insulated magnet.

Upon reaching the target excitation current, the azimuthal current within the NI magnet continues to increase, preventing a sudden change in the amplitude of the SCIF. On the one hand, the radial current decays, causing the azimuthal currents of all turns to approach the target current. On the other hand, the relaxation of the screening current in the axial direction leads to a more uniform current density distribution. These combined effects cause a drift in the central magnetic field. In general, it is the directional and magnitude variations of the azimuthal current within different DP coils that lead to a different trend in the SCIF for the NI superconducting magnet as compared to the insulated magnet. Certain amounts of reversed current persist even after the insert coil has been excited for some time. This indicates the possibility of reversed currents persisting even when both the insert coil and the background field coil are simultaneously excited.

4.2 Comparison of SCIS

For UHF REBCO magnets, the screening current-induced stress (SCIS) is non-negligible. As the variations in screening current due to reverse currents differ between NI and insulated superconducting magnets, the stress in these magnets may differ as well. We import the Lorentz forces calculated from the electromagnetic module into a 2D axisymmetric solid mechanics module in COMSOL Multiphysics. Since the high-field REBCO coils are wound using a dry winding method, with no epoxy resin adhesive between turns, adjacent turns may either contact or separate during excitation. This non-linear problem induced by the potential contact or separation of turns was addressed using the "Contact Pair" and an in-built penalty function method available in COMSOL Multiphysics. The conductor thickness may affect the calculated stress magnitude, we modeled the geometric shapes of each turn, winding bobbin, and overbanding, rather than simplifying multiple conductors turns into a single engineering turn. It is impractical to accurately establish all contact pairs in the entire magnet at once, so we calculated each SP coil separately, forcing the axial displacement at the bottom edge of each SP coil to be zero, while the other boundaries could move freely, achieved via the "Roller" condition applied to the entire bottom edge.

The frictional force significantly influences the calculated results by impeding radial displacement at each turn. As this force is directly associated with the axial compressive stress between the SP coils, we first calculated the axial Lorentz force for each individually SP coil. When calculating a specific SP coil, we applied the accumulated axial Lorentz force from all upper SP coils, multiplied by the friction coefficient, at the contact point between the SP coil and the spacer. To maintain zero net force, the frictional forces acting on each interface were in opposite directions, but of equal magnitude. The equations are as follows:

$$\begin{cases} f_i^t = \mu\left(P^p + \sum_{j=1}^{i-1} P_i^L\right), \\ f_i^b = \mu\left(P^p + \sum_{j=1}^{i} P_i^L\right), \end{cases} \tag{22}$$

where f_i^t and f_i^b represent the friction forces acting on the top and bottom edges of the i-th SP coil, respectively, μ is the friction coefficient, P^p is the pressure generated by the pre-tensioning force, and P_i^L is the pressure generated by the axial Lorentz force.

In our research, we chose a friction coefficient of 0.2, and referred to the ref. [35] to determine parameters such as Young's modulus and Poisson's ratio for various materials.

As illustrated in Figure 10, at the respective maximum hoop stress points of the NI and insulated magnets, the distributions of their radial Lorentz force f_r, axial Lorentz force f_z, and hoop stress exhibit similar patterns. The hoop stress primarily behaves as tensile stress on the outer side and as compressive stress on the inner side. However, the insulated magnet reaches a maximum hoop stress of 1285 MPa at 7200 s, with a corresponding central magnetic field of 31.89 T, while the NI magnet's maximum hoop stress of 1172 MPa occurs at 8510 s, with a central magnetic field of 30.79 T at that moment. Interestingly, both the radial and axial Lorentz forces in the NI magnet are somewhat lower than those in the insulated magnet, which might be attributed to the reversed current experienced in the NI magnet. Furthermore, the maximum hoop stress in the NI magnet is not reached after the magnetic field stabilizes, but beforehand. This is because the magnetic field continues to grow after the current reaches its target value, and both the critical current and screening current are reducing, thereby causing a peak in the Lorentz force. As depicted in Figure 11, the maximum hoop stress in each DP coil presents noticeable discrepancies between the insulated and NI magnets. Except for a few DP coils near the mid-plane, the hoop stress in all other coils within the NI magnet is lower than those in the insulated magnet.

The maximum hoop SCIS in Figures 10 and 11 exceeds 1 GPa, while the irreversible tensile stress for typical REBCO tape is usually around 800 MPa [36]. In most of the

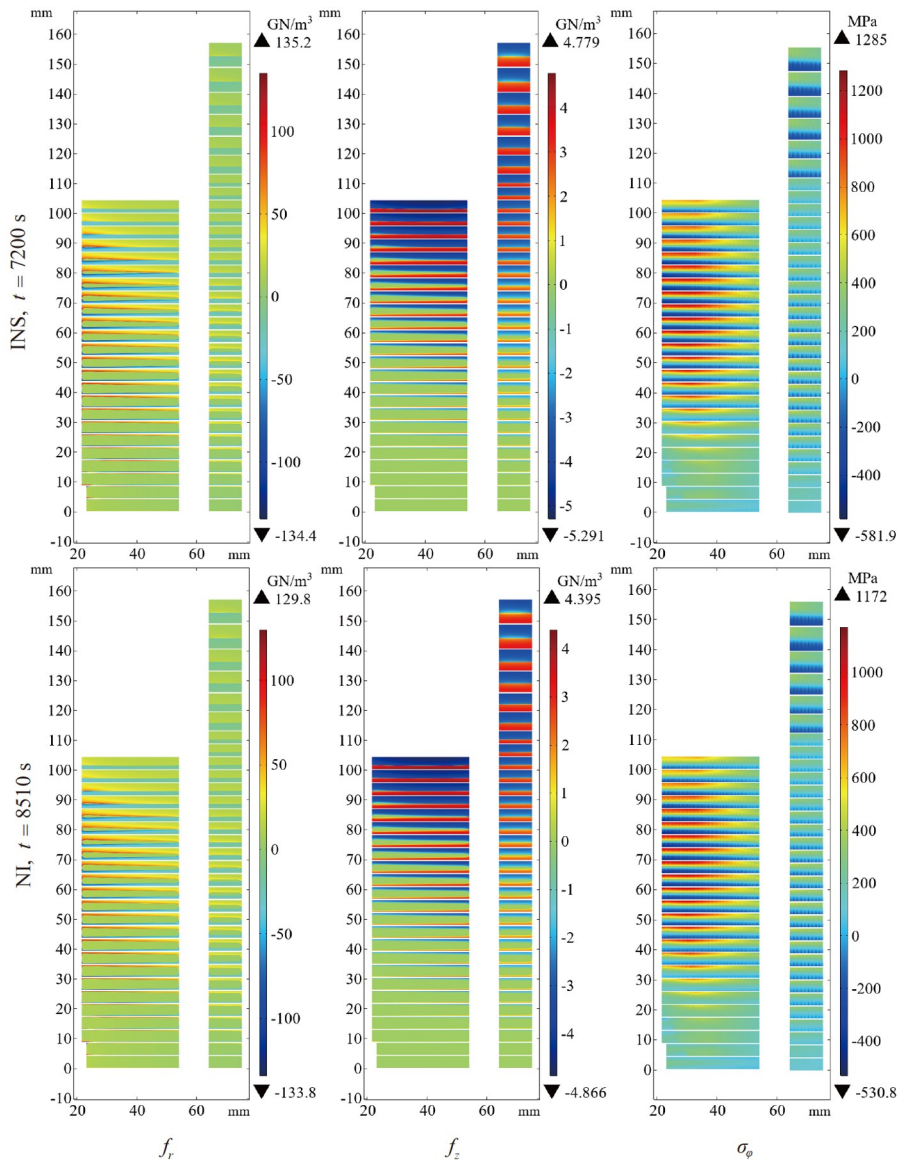

Figure 10 (Color online) Comparison of Lorentz force and hoop stress between NI and insulated magnets.

current research, stress calculated solely from the screening current often exceeds 800 MPa or surpasses experimental measurements [5,37–39]. Some studies have considered factors such as strain and rotation effects, leading to more realistic values for critical current, *n*-values, and contact resistance [40–43]. However, the computed values for the SCIS still tend to exceed actual values. Additionally, the inward winding of the superconducting layers induces compressive bending strain. Pre-stressing and over-banding [44] can further reduce stress in the coil, potentially maintaining the actual stress within the irreversible stress range for superconducting magnets. Given the computational challenges of simultaneously considering tens of thousands of turns in the coil with rotation effects and elastic-plastic behavior, and since bending strain, pre-stressing, and over-banding are fixed, the main purpose of Figures 10 and 11 is to demonstrate the relative differences of SCIS between NI and INS magnet. Therefore, this study focuses solely on stress induced by screening current, without considering other complex factors.

4.3 Comparison of SCIF and losses during field sweeps

We simulated the SCIF and losses during the field sweeps. Unlike the typical field sweeps between positive target fields and negative target fields, the operating mode of the magnet in this study involves field sweeps between zero field and a positive target field, with a period of maintenance at the positive target field as shown in Figure 11. This process involves six stages across three cycles. During the excitation

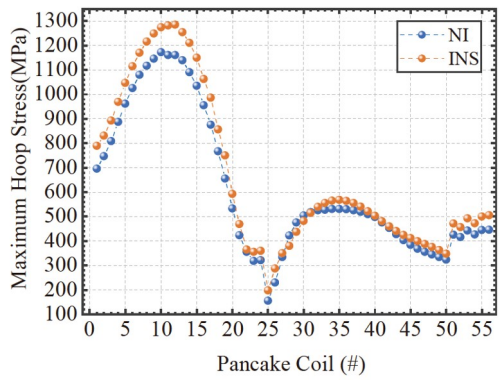

Figure 11 Comparison of maximum hoop stresses in each DP coil between NI magnet and insulated magnet. The DP coils are numbered as follows: the end DP coil in the inner insert is labeled as coil 1, the middle DP coil in the inner insert is labeled as coil 24, the middle DP coil in the outer insert is labeled as coil 25, and the end DP coil in the outer insert is labeled as coil 56.

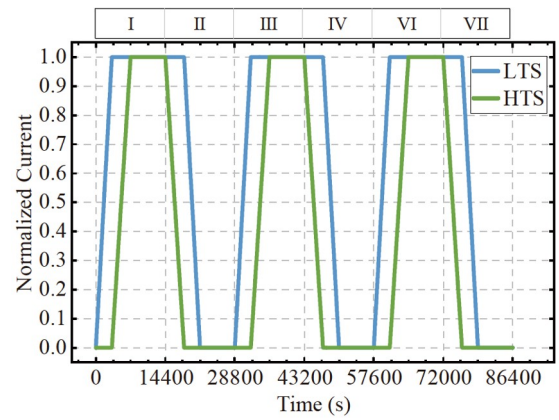

Figure 12 Schematic diagram of the current variation during the field sweeping process. The simulation consists of three sweep cycles, each comprising two stages: excitation and discharging.

stage, the LTS background coil begins charging, followed by the HTS insert coil, taking a total of 2 h to reach the target current. During discharging stage, the HTS insert coil begins discharging, followed by the LTS background coil, taking a total of 2 h to decrease the current to zero. Following the attainment of the target current and the zero current, each is maintained for a period of 2 h.

Figure 12 illustrates the responses of the SCIF in both the NI and insulated magnets as functions of the central magnetic field. For both types of magnets, a hysteresis loop is formed after each stage following the first stage. Although the hysteresis loops do not coincide, the gap between them narrows as the number of sweep cycles increases. This suggests that the present central magnetic field can be obtained through the present current and the previously calibrated magnet constant, even though the magnet constant is nonlinear and the magnet has gone through multiple sweep cycles.

When the current is maintained stable, the relaxing screening current consistently drives the SCIF towards zero, resulting in a drift in the central magnetic field. The direction of this drift is opposite to the direction of the SCIF. Interestingly, at an identical central magnetic field, the SCIF of the NI magnet is always smaller than that of the insulated magnet. This could be related to the reverse current in the NI magnet, which creates an effect similar to current sweep reversal.

The loss power P during the field sweeping process is determined by the current density J and electric field E, and can be represented by the following:

$$P = \mathbf{E} \cdot \mathbf{J} = E_\varphi J_\varphi + E_r J_r, \tag{23}$$

where $E_\varphi J_\varphi$ represents the hysteresis loss, which is the only type of loss in insulated magnets. $E_r J_r$ is caused by the inter-turn resistance, mainly arising from the contact resistance, so we call it the inter-turn contact loss. NI magnets have both hysteresis loss and inter-turn contact loss. The total loss is obtained through the spatial integration of power density over the coil and time integration over the entire field sweeping cycle:

$$Q = \int_T \mathrm{d}t \int_\Omega 2\pi r E \cdot J \mathrm{d}\Omega. \tag{24}$$

Figure 13 shows the changes in loss power throughout the field sweeping cycle. For hysteresis loss, after the first cycle, the pattern of loss in subsequent field sweeping cycles remains consistent, with a characteristic feature being that the discharging stage experiences more loss than the excitation stage. Regarding inter-turn contact loss, the pattern across each cycle is nearly the same, with the discharging stage having slightly more loss than the excitation stage. Owing to the magnetic field delay caused by the inter-turn bypass current, the hysteresis loss of the NI magnet consistently lags behind that of the insulated magnet. However, it is noteworthy that the peak power of contact loss induced by the inter-turn bypass current exceeds the peak power of hysteresis loss by over 30 times.

After the first excitation stage, the hysteresis loss in the insulated insert coil caused due to the change in the background field is less than the hysteresis loss caused by the change in the self-field of the insert coil. Therefore, the loss curve abruptly rises when the background coil excitation ends and the insert coil begins its excitation. The total hysteresis loss for the insulated insert coil is Q = 5.54 kJ, with the hysteresis losses during the background coil excitation, insert coil excitation, and current maintenance stages accounting for 24.0%, 68.1%, and 7.9%, respectively. For the NI magnet, after the end of the background excitation, the induced reverse current rapidly transitions into the positive current driven by the power supply when the insert coil starts its excitation, causing the hysteresis loss sharply decreases and the inter-turn contact loss sharply rises. The total

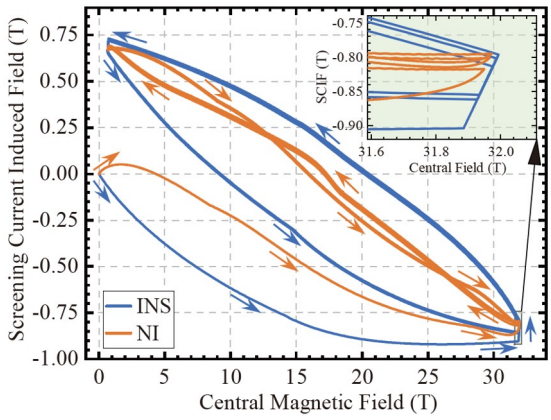

Figure 13 Comparison of SCIF between the NI magnet and the insulated magnet during three field sweeping cycles.

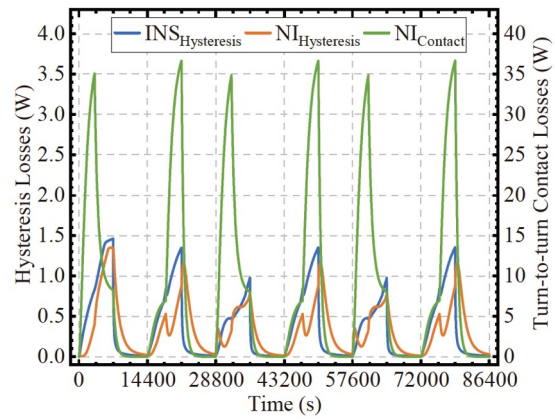

Figure 14 Comparison of loss between the NI magnet and the insulated magnet during three field sweeping cycles.

hysteresis loss for the NI magnet is Q = 4.99 kJ, with the hysteresis losses during the background excitation, insert excitation, and current maintenance stages accounting for 13.5%, 35.8%, and 50.7% respectively. The total inter-turn contact loss is Q = 126.48 kJ, with the corresponding losses accounting for 11.9%, 73.2%, and 14.9%, respectively.

5 Discussion

In Section 2, the numerical model makes a rotational transformation from the perspective of logical reasoning. Due to the limitation of the bending radius of the superconducting coil, $\frac{d}{2\pi r}$ is a very small value, so the rotation angle is close to zero. Therefore, even without making a rotation transformation and directly setting $J_{\parallel} = J_{\varphi}$ and $J_{\perp} = J_r$, the results will not vary significantly. We introduce an index to measure the difference between $J_{\parallel}$ and J_{φ}, defined as their maximum relative error $\varepsilon_{\max} = \max\left(\left|\frac{J_{\parallel}-J_{\varphi}}{J_{\parallel}}\right|\right)$. J_{φ} is related to θ and J_r. At t = 3314 s, J_r is at its maximum, and at t = 14400 s, J_r is at its minimum. Therefore, we compared the maximum relative error of the current density on the cross-section at different circumferential positions at t = 3314 s and t = 14400 s. The results are shown in Figure 14. Even when the radial current density J_r is very large, the maximum relative error of the current density is only 21.51 ppm.

Therefore, for the calculation of screening current in NI superconducting coils, the 2D axisymmetric coordinates can be used directly without coordinate transformation. This can greatly improve the calculation speed without sacrificing accuracy. Using a commercial desktop computer (16 cores, AMD 7950X 3D, 5.8 GHz, 128 GB RAM) to simulate the liquid helium experiment process in Figure 6 from the 49th hour to the 89th hour, if 2D axisymmetric coordinates are used directly, it takes 58491 s to simulate the 144000 s' liquid helium experiment. This enables real-time simulation of screening current in a high-field un-insulated superconducting magnet with tens of thousands of turns.

The key to establishing the relationship between the radial current density and the circumferential current density of the un-insulated superconducting coil in this paper is to solve for $\frac{\partial A_{\varphi}}{\partial t}$. Since the **T-A** formulation uses **A** as the dependent variable throughout the domain, it is convenient to solve for $\frac{\partial A_{\varphi}}{\partial t}$ in the superconducting domain. For some materials such as Bi-223 and MgB_2, they cannot be simplified to a 1D thin layer due to their inherent structural characteristics. Typically, the **H-A** formulation, **H-Φ** formulation, and other subdomain solutions or direct use of the **H** formulation are applied. However, given the absence of variable A in the superconducting domain of those formulation, it is not possible to directly solve for $\frac{\partial A_{\varphi}}{\partial t}$.

In order to address this, we can introduce the magnetic flux Φ as an intermediate variable:

$$\int_a^b \frac{\partial A}{\partial t}\mathrm{d}l \approx \iint_S \nabla \times \frac{\partial A}{\partial t}\mathrm{d}S = \frac{\partial \Phi}{\partial t}. \tag{25}$$

Magnetic flux Φ can be expressed as a spatial integral of the axial component of the magnetic field:

$$\Phi = \mu \int\int_0^r 2\pi r H_z \mathrm{d}r. \tag{26}$$

Therefore, the axial component of the magnetic field can be directly utilized in the superconducting domain to acquire the relationship between the radial current density and the azimuthal current density:

$$J_r = \frac{\frac{\partial \Phi}{\partial t} + 2\pi r \cdot \rho_{\varphi} J_{\varphi}}{d \cdot \rho_r}. \tag{27}$$

In COMSOL Multiphysics, we can solve the spatial

integral in eq. (26) by adding a custom PDE:

$$\frac{\partial \Phi}{\partial r} = 2\pi r \mu H_z. \tag{28}$$

Extensive research has been undertaken by various institutions to understand the damage caused by SCIS in superconducting magnets. NHMFL has developed a series of REBCO coils and placed them in a background field exceeding 30 T, resulting in magnetic fields of over 40 T [39]. When the outer edge of the REBCO coil is a slit edge, damage to the conductor can often be observed, particularly in the buffer layer and the REBCO layer at the slit edges. However, such damage is not present when current flows along the non-slit edge. Similar phenomena were also observed in the study by Takahashi et al. [45], indicating a connection with pre-cracks in the outer edge and excessive tensile hoop stress induced by the screening current. As a result, designers tend to position the slit edges on the inner side to reduce the influence of tensile hoop stress on pre-cracks at the slit edges, as shown in Figure 16(a). However, this work shows that the reverse-induced current during the excitation process of NI magnet will generate a reverse screening current, which may cause tensile hoop stress on the inner side rather than the conventional compressive hoop stress, as shown in Figure 16(b). While under the specific conditions and magnet configurations explored in this study, significant tensile hoop stress on the magnet's inner side will not occur, such a phenomenon may indeed arise in NI superconducting magnets under certain circumstances. Presently, LTS magnets can achieve more than 20 T, and the inter-turn contact resistivity of NI coils ranges from several $\mu\Omega\ \mathrm{cm}^2$ to several thousand $\mu\Omega\ \mathrm{cm}^2$ [46]. Therefore, we assume that the background coil of this magnet in this paper has a field of 20 T, and the inter-turn contact resistivity is 1 $\mu\Omega\ \mathrm{cm}^2$, with other parameters and the stress calculation model remaining unchanged. Under this assumption, significant tensile/compressive hoop stress would arise on the inside/outside of the HTS DP coil when reverse screening current is generated. Figure 17 shows the hoop stress distribution of the end DP coil of the inner insert. At $t = 5005$ s, the compressive hoop stress on the outside reaches its peak at −480 MPa, and the tensile hoop stress on the inside reaches 561 MPa. This might exacerbate the damage to the slit edge position on the magnet's inner side. Particularly during NI magnet quench, the mutual induction between non-quenched DP coils could lead to more complex SCIS.

6 Conclusions

This work introduces a novel method based on the homogenized **T-A** formulation, for enabling real-time simulations of the bypass current and screening current effects of NI superconducting magnets encompassing tens of thousands of turns, by representing the radial current density as a function of the azimuthal current density. This method has been substantiated through liquid nitrogen and liquid helium experimental evaluations. Utilizing this method, the discrepancies in the screening currents of 32 T NI superconducting magnets and insulated superconducting magnets were investigated, resulting in the following conclusions.

(1) During the excitation of background field coils, a current opposite to the direction of the operating current driven by the power source is induced in the NI insert superconducting coils. This results in a screening current

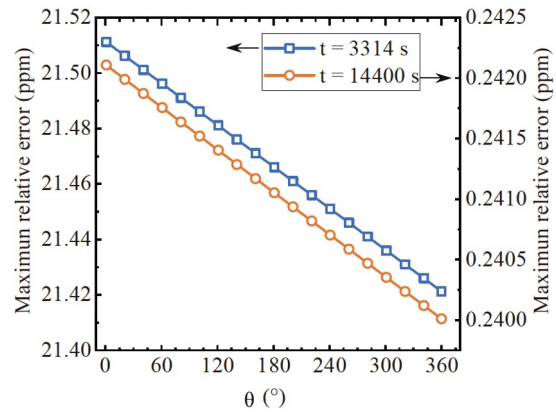

Figure 15 (Color online) Comparison of the maximum relative error of current density when the coordinates are transformed and not transformed.

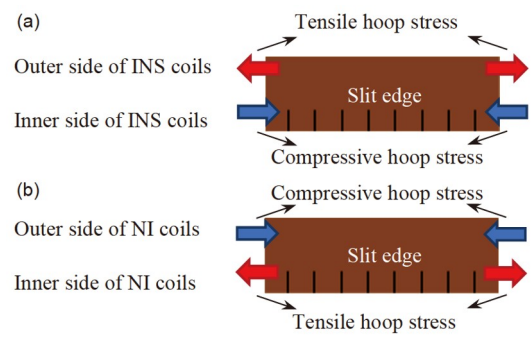

Figure 16 (Color online) Schematic diagram of the reverse hoop stress in the NI coil. (a) Compressive hoop stress on the slit edge of the INS coil; (b) tensile hoop stress on the slit edge of the NI coil.

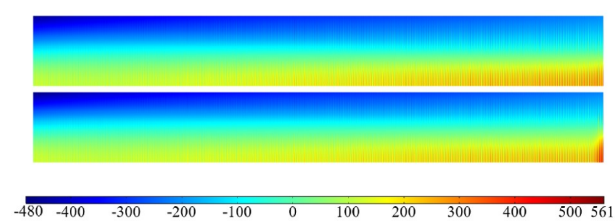

Figure 17 (Color online) Hoop stress of the end coil in the inner NI insert magnet (Unit: MPa).

distribution within the non-insulated superconducting coils that is opposite to that found within the insulated superconducting coils. Consequently, the NI magnet exhibits variations in the SCIF, screening current-induced stress, and losses when compared to the insulated magnet.

(2) For the magnet parameters discussed in this study, the peak screening current-induced stress in the NI superconducting magnet is less than that in the insulated superconducting magnet, with this peak stress in the NI superconducting magnet arising prior to the magnetic field reaching its maximum value. Therefore, the stress at the point of attaining the target magnetic field cannot be considered as the basis for the magnet's design.

(3) After undergoing numerous cycles of field sweeping, the hysteresis curves of each cycle nearly coincide. Moreover, when the central magnetic field is the same, the SCIF of the NI superconducting magnet remains consistently lesser than that of the insulated superconducting magnet.

(4) The presence of radial current leads to the hysteresis loss of the NI superconducting magnet falling behind that of the insulated superconducting magnet. The hysteresis loss in the insulated superconducting magnet is predominantly seen during the insert coil excitation phase, whereas, in the case of the NI superconducting magnet, it is chiefly observed during the current hold phase.

The screening current is significantly influenced by the critical current, which is affected not only by the magnetic field but also by temperature and stress. To precisely calculate the screening current of high-field NI superconducting magnets, it is crucial to establish a multi-physics coupled model incorporating mechanical, electromagnetic, and thermal phenomena. This forms the central theme of our future research. Furthermore, the key distinction between NI superconducting magnets and insulated superconducting magnets is the inter-turn resistivity. Consequently, our future work will involve studying the screening current of NI superconducting magnets with varying inter-turn resistivities under diverse excitation speeds.

We wish to thank Li Lv, Jianlin Luo, Pu Wang, Gang Li, Zheng Li and Guozhi Fan from the Institute of Physics, Chinese Academy of Sciences for their assistance. This work was supported by the National Key Research and Development Program of China (Grant No. 2022YFA1602800), the National Natural Science Foundation of China (Grant Nos. 52325701, 52293421, 52293422, and 52293423), and the Synergetic Extreme Condition User Facility (SECUF) Project.

1 National Research Council. High Magnetic Field Science and Its Application in the United States. Washington: National Academies Press, 2013
2 Senatore C, Alessandrini M, Lucarelli A, et al. Progresses and challenges in the development of high-field solenoidal magnets based on RE123 coated conductors. Supercond Sci Tech, 2014, 27: 103001
3 Uglietti D, Yanagisawa Y, Maeda H, et al. Measurements of magnetic field induced by screening currents in YBCO solenoid coils. Supercond Sci Tech, 2010, 23: 115002
4 Yanagisawa Y, Kominato Y, Nakagome H, et al. Magnitude of the screening field for YBCO coils. IEEE Trans Appl Supercond, 2011, 21: 1640–1643
5 Xia J, Bai H, Yong H, et al. Stress and strain analysis of a REBCO high field coil based on the distribution of shielding current. Supercond Sci Tech, 2019, 32: 095005
6 Yang Z, Li Y, Song P, et al. Effect of edge cracks on critical current degradation in REBCO tapes under tensile stress. Superconductivity, 2022, 1: 100007
7 Huber F, Song W, Zhang M, et al. The ***T-A*** formulation: An efficient approach to model the macroscopic electromagnetic behaviour of HTS coated conductor applications. Supercond Sci Tech, 2022, 35: 043003
8 Rhyner J. Magnetic properties and AC-losses of superconductors with power law current-voltage characteristics. Physica C-Supercond, 1993, 212: 292–300
9 Berrospe-Juarez E, Zermeño V M R, Trillaud F, et al. Real-time simulation of large-scale HTS systems: Multi-scale and homogeneous models using the ***T-A*** formulation. Supercond Sci Tech, 2019, 32: 065003
10 Hahn S, Park D K, Bascunan J, et al. HTS pancake coils without turn-to-turn insulation. IEEE Trans Appl Supercond, 2011, 21: 1592–1595
11 Liu J, Wang Q, Qin L, et al. World record 32.35 tesla direct-current magnetic field generated with an all-superconducting magnet. Supercond Sci Tech, 2020, 33: 03LT01
12 Hahn S, Kim K, Kim K, et al. 45.5-Tesla direct-current magnetic field generated with a high-temperature superconducting magnet. Nature, 2019, 570: 496–499
13 Yanagisawa Y, Sato K, Yanagisawa K, et al. Basic mechanism of self-healing from thermal runaway for uninsulated REBCO pancake coils. Physica C-Supercond, 2014, 499: 40–44
14 Wang Y, Song H, Xu D, et al. An equivalent circuit grid model for no-insulation HTS pancake coils. Supercond Sci Tech, 2015, 28: 045017
15 Wang Y, Kan Chan W, Schwartz J. Self-protection mechanisms in no-insulation (RE)$Ba_2Cu_3O_x$ high temperature superconductor pancake coils. Supercond Sci Tech, 2016, 29: 045007
16 Liu D, Zhang W, Yong H, et al. Thermal stability and mechanical behavior in no-insulation high-temperature superconducting pancake coils. Supercond Sci Tech, 2018, 31: 085010
17 Lee J, Park D, Michael P C, et al. A field-shaking system to reduce the screening-current-induced field in the 800-MHz HTS insert of the MIT 1.3-GHz LTS/HTS NMR magnet: A small-model study. IEEE Trans Appl Supercond, 2018, 28: 1–5
18 Wei J, Huang Z, Lei Z, et al. Study on helium gas bubble levitation in high field superconducting magnet. Supercond Sci Tech, 2023, 36: 095011
19 Li Y, Park D, Lee W, et al. Screening-current-induced strain gradient on REBCO conductor: An experimental and analytical study with small coils wound with monofilament and striated multifilament REBCO tapes. IEEE Trans Appl Supercond, 2020, 30: 1–5
20 Wang L, Wang Q, Liu J, et al. Screening current-induced magnetic field in a noninsulated GdBCO HTS coil for a 24 T all-superconducting magnet. IEEE Trans Appl Supercond, 2017, 27: 1–6
21 Bean C P. Magnetization of hard superconductors. Phys Rev Lett, 1962, 8: 250–253
22 Bean C P. Magnetization of high-field superconductors. Rev Mod Phys, 1964, 36: 31–39
23 Qin L, Wang L, Liu J, et al. Refined circuit model for current distribution of the no-insulation HTS insert magnet. Supercond Sci Tech, 2021, 34: 075002
24 Noguchi S, Imai T, Park D, et al. A simple screening current simulation method using equivalent circuit model for REBCO pancake coils. Supercond Sci Tech, 2020, 33: 115005
25 Mataira R C, Ainslie M D, Badcock R A, et al. Finite-element modelling of no-insulation HTS coils using rotated anisotropic resistivity. Supercond Sci Tech, 2020, 33: 08LT01
26 Berrospe-Juarez E, Trillaud F, Zermeno V M R, et al. Screening currents and hysteresis losses in the REBCO insert of the 32 T all-

superconducting magnet using ***T-A*** homogenous model. IEEE Trans Appl Supercond, 2020, 30: 1–5
27 Otten S, Kario A, Demenčik E, et al. Anisotropic monoblock model for computing AC loss in partially coupled Roebel cables. Supercond Sci Tech, 2020, 33: 094013
28 Zhang H, Zhang M, Yuan W. An efficient 3D finite element method model based on the ***T-A*** formulation for superconducting coated conductors. Supercond Sci Tech, 2017, 30: 024005
29 Berrospe-Juarez E, Trillaud F, Zermeño V M R, et al. Advanced electromagnetic modeling of large-scale high-temperature superconductor systems based on *H* and *T-A* formulations. Supercond Sci Tech, 2021, 34: 044002
30 Zermeño V M R, Habelok K, Stępień M, et al. A parameter-free method to extract the superconductor's J_c (B, θ) field-dependence from in-field current-voltage characteristics of high temperature superconductor tapes. Supercond Sci Tech, 2017, 30: 034001
31 Hilton D K, Gavrilin A V, Trociewitz U P. Practical fit functions for transport critical current versus field magnitude and angle data from (RE)BCO coated conductors at fixed low temperatures and in high magnetic fields. Supercond Sci Tech, 2015, 28: 074002
32 Wimbush S C, Strickland N M. A public database of high-temperature superconductor critical current data. IEEE Trans Appl Supercond, 2017, 27: 1–5
33 Barth C, Mondonico G, Senatore C. Electro-mechanical properties of REBCO coated conductors from various industrial manufacturers at 77 K, self-field and 4.2 K, 19 T. Supercond Sci Tech, 2015, 28: 045011
34 Zhou B, Wang L, Wang K, et al. Experimental and simulation studies of SCIF considering non-uniform critical current. Supercond Sci Tech, 2022, 35: 075002
35 Wang L, Wang Q, Li L, et al. Stress analysis of winding process, cooling down, and excitation in a 10.7 T REBCO HTS magnet. IEEE Trans Appl Supercond, 2018, 28: 1–5
36 Zhang Y, Hazelton D W, Kelley R, et al. Stress-strain relationship, critical strain (stress) and irreversible strain (stress) of IBAD-MOCVD-based 2G HTS wires under uniaxial tension. IEEE Trans Appl Supercond, 2016, 26: 1–6
37 Li Y, Park D, Yan Y, et al. Magnetization and screening current in an 800 MHz (18.8 T) REBCO nuclear magnetic resonance insert magnet: Experimental results and numerical analysis. Supercond Sci Tech, 2019, 32: 105007
38 Park D, Bascunan J, Li Y, et al. Design overview of the MIT 1.3-GHz LTS/HTS NMR magnet with a new REBCO insert. IEEE Trans Appl Supercond, 2021, 31: 1–6
39 Hu X, Small M, Kim K, et al. Analyses of the plastic deformation of coated conductors deconstructed from ultra-high field test coils. Supercond Sci Tech, 2020, 33: 095012
40 Yan Y, Song P, Xin C, et al. Screening-current-induced mechanical strains in REBCO insert coils. Supercond Sci Tech, 2021, 34: 085012
41 Kolb-Bond D, Bird M, Dixon I R, et al. Screening current rotation effects: SCIF and strain in REBCO magnets. Supercond Sci Tech, 2021, 34: 095004
42 Niu M, Xia J, Yong H. Numerical analysis of the electromechanical behavior of high-field REBCO coils in all-superconducting magnets. Supercond Sci Tech, 2021, 34: 115005
43 Li D, Tang Y, Liu D, et al. Numerical analysis of the contact resistance in a no-insulation layer-wound coil with a simplified electromagnetic–mechanical model. Supercond Sci Tech, 2022, 35: 124004
44 Guan M, Hahn S, Bascunan J, et al. A parametric study on overband radial build for a REBCO 800-MHz insert of a 1.3-GHz LTS/HTS NMR magnet. IEEE Trans Appl Supercond, 2016, 26: 1–5
45 Takahashi S, Suetomi Y, Takao T, et al. Hoop stress modification, stress hysteresis and degradation of a REBCO coil due to the screening current under external magnetic field cycling. IEEE Trans Appl Supercond, 2020, 30: 1–7
46 Zhang H, Suo H, Wang L, et al. Database of the effect of stabilizer on the resistivity and thermal conductivity of 20 different commercial REBCO tapes. Supercond Sci Tech, 2022, 35: 045016